First mixed-valence Cu II /Cu I coordination polymer based on 2,5-bis(pyridine-2-yl)-1,3,4-thiadiazole and thiocyanate: Synthesis, structural characterization and antimicrobial in vitro activity assessment

Abdelhakim Laachir, Salaheddine Guesmi, Hanane Zine, Mohammed Faize, El Mostafa Ketatni, Mohamed Saadi, Lahcen El Ammari, Olivier Mentré, Fouad Bentiss

First mixed-valence Cu^{II}/Cu^{I} coordination polymer based on 2,5-bis(pyridine-2-yl)-1,3,4-thiadiazole and thiocyanate: Synthesis, structural characterization and antimicrobial in vitro activity assessment

Abdelhakim Laachir [a], Salaheddine Guesmi [a], Hanane Zine [b], Mohammed Faize [b], El Mostafa Ketatni [c], Mohamed Saadi [d], Lahcen El Ammari [d], Olivier Mentré [e], Fouad Bentiss [f,*]

[a] *Laboratory of Coordination and Analytical Chemistry (LCCA), Faculty of Sciences, Chouaib Doukkali University, PO Box 20, M-24000 El Jadida, Morocco*
[b] *Laboratory of Plant Biotechnology, Ecology and Ecosystem Valorization, Faculty of Sciences, Chouaib Doukkali University, PO Box 20, M-24000 El Jadadia, Morocco*
[c] *Laboratory of Organic and Analytical Chemistry, Faculty of Science and Technology, Sultan Moulay Slimane University, PO Box 523, Beni-Mellal, Morocco*
[d] *Laboratoire de Chimie Appliquée des Matériaux, Centre des Sciences des Matériaux, Faculty of Science, Mohammed V University in Rabat, Avenue Ibn Batouta, B.P. 1014, Rabat, Morocco*
[e] *Univ. Lille, CNRS, Centrale Lille, UMR 8181, - UCCS - Unité de Catalyse et de Chimie du Solide, F-59000 Lille, France*
[f] *Laboratory of Catalysis and Corrosion of Materials (LCCM), Faculty of Sciences, Chouaib Doukkali University, PO Box 20, M-24000 El Jadida, Morocco*

* Corresponding author. fbentiss@gmail.com

ABSTRACT

While this new polymer exhibited a noticeable activity against the phytopathogenic bacteria *Agrobacterium tumefaciens* no significant activity was recorded against *Pseudomonas syringae pv. syringae* and *Pseudomonas syringae* pv. *tobacco* nor against the phytopathogenic fungi *Verticillium dahlia* and *Fusarium oxysporum* fsp. *melonis*.

Keywords: 2,5-Bis(pyridin-2-yl)-1,3,4-thiadiazole; C^{II}/Cu^{I} polymeric complex; Crystal structure; Hirshfeld surface analysis; Antiphytopathogenic activity.

1. Introduction

In recent years, coordination polymers (CPs) have attracted great interest by their applications in various fields such as biology [1,2], catalysis [3,4] or magnetism [5,6]. Among these CPs, a class called metal-organic frameworks (MOFs), was distinguished by its porosity, in the field of storage [7,8] and purification of gases [9,10]. One of the strategies that was deployed for the synthesis of such systems was the assembly of nodes, consisting of metallic entities (atoms or molecules) with organic bridging ligands [11,12]. This method allowed access to mono-, bi- or three-dimensional materials with interesting physical properties, in particular with hetero cyclic ligands such as pyridine [13,14], imidazole [15,16] or thiadiazole [17-19]. In this field, coordination complexes constructed from metal centers and the dipyridyl bridging ligand, 2,5-bis(pyridine-2-yl)-1,3,4-thiadiazole (noted L) have attracted attention by their potential supramolecular architectures. However, the organic ligand L although it has shown the ability to bridge metal sites and generate bimetallic (mode b or c in Fig. 1) [20-22] or polymeric complexes [23], it has above all a tendency to chelate a metal and lead to trans mononuclear complexes of ML_2X_2 type (mode a) [24-27]. In fact, to our knowledge, only one polymer of formula $[CuLCl_2]_n$ has been isolated by our team in which the ligand L adopts the bridging mode d as described in Fig. 1.

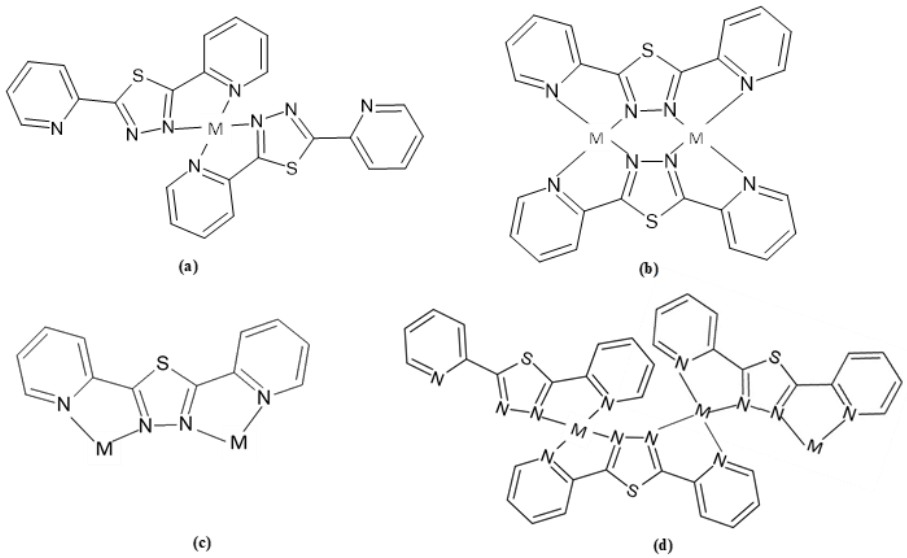

Fig. 1. The known coordination modes of 2,5-bis(pyridine-2-yl)-1,3,4-thiadiazole (**L**).

With divalent copper, several mono or bimetallic complexes have been obtained in our laboratory, with or without pseudo halides as coligands and they have shown magnetic properties [25,28] and biological activities [23,29]. With the azide N_3^-, a complex of formula $Cu_2L_2(N_3)_4$ was obtained and its structure shows a one-dimensional Cu(II) zigzag chain generated by alternating two Cu–Cu distances with alternating antiferromagnetic exchange couplings [28].The latter exhibits in addition an excellent antifungal activity against *Verticillium dahliae* [29]. With the thiocyanate NCS^-, a monometallic complex was obtained in which the coligand is linked via the sulfur atom [30]. But our choice was focused on thiocyanate as coligand because it's an ambidentate ligand, very flexible that can coordinate either through the sulfur atom S [31,32], either by the nitrogen atom N [33,34], or both at the same time and thus lead to polymetallic or polymeric complexes (Fig. 2.) [32,35]. Current studies show that metal complexes containing thiocyanate are among the most studied systems due to the diversity of their structures and applications in the field of materials sciences [36-38]. In addition, we were interested in coligand thiocyanate because it is well known that thiocyanate can also partially reduce *in situ*, Cu^{II} to Cu^{I} and thus leads to mixed valence Cu(I/II)-thiocyanate coordination polymers. This type of mixed-valence complex is more interesting than those of Fe or Co because the copper (I) and copper (II) metal centers prefer different geometries and the two oxidation states are very labile and stereo chemically flexible [39,40]. On the other hand, the chemistry of mixed-valence Cu^{II}/Cu^{I} coordination complexes are gaining popularity due to its great applications in various fields like as biological activity [41,42], electronic properties [43,44] and electrical conductivity [45,46]. Although, a first attempt in this context, only a monometallic complex of formula $[CuL_2(SCN)_2]$ was isolated [30], we present here the synthesis and characterization of the first mixed-valence coordination polymer, $[Cu^{I}_3Cu^{II}L_2(SCN)_5]_n$, based on L as ligand and thiocyanate as coligand, after a small

modification of the preparation method. Its biological activity was also accessed against some fungal and bacterial phytopathogens.

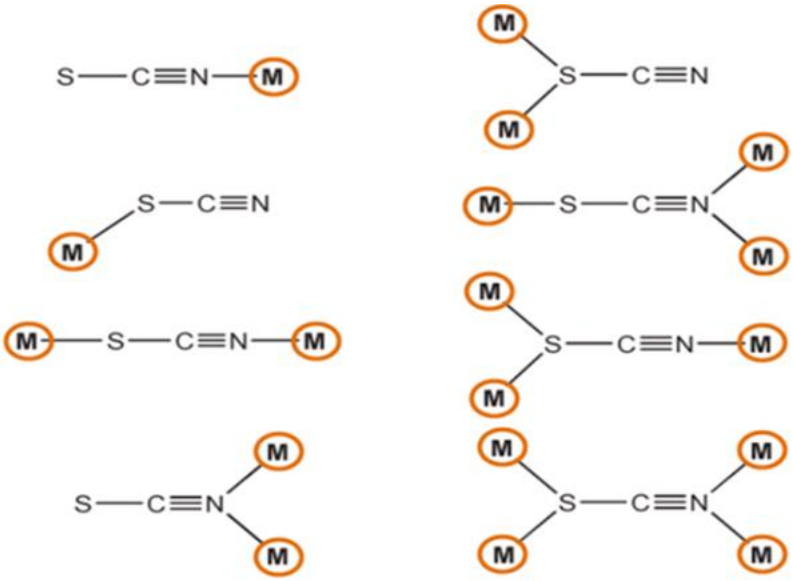

Fig. 2. Different coordination modes of thiocyanato ligand.

2. Experimental

2.1. Materials

All the solvents and reagents for synthesis were commercially available and used as received.

2.1.1. Synthesis of 2,5-bis(pyridine-2-yl)-1,3,4-thiadiazole (L)

The ligand, namely 2,5-bis(pyridine-2-yl)-1,3,4-thiadiazole (L) was synthesized according to the literature procedure [47]. The molecular structure of L was confirmed by ^{1}H NMR, ^{13}C NMR, and elemental analyses. Yield: 62%, m.p.: 218°C. ^{1}H NMR (300 MHz, DMSO-d_6): δ(ppm) 7.59 (2H, d), 8.03 (2H, d), 8.31 (2H, t), 8.73 (2H, t). ^{13}C NMR (75 MHz, DMSO-d_6): δ(ppm) 171.14, 150.30, 148.17, 138.02, 126.22, 120.56. Anal. Calcd for $C_{12}H_8N_4S$: C, 59.98; H, 3.36; N, 23.32; S, 13,34. Found: C, 60.13; H, 3.25; N, 23.28, S, 13,48. IR (KBr

pellet, cm^{-1}): 3058 (W), 1580 (vs), 1560 (s), 1427 (vs), 637 (w); UV-vis (λ_{max}, nm (ε_{max}, M^{-1} cm^{-1}) in DMSO (10^{-4} M) solvent 305 (15700) ; 245 (11810).

2.1.2. Synthesis of title complex: $[Cu^{I}_3Cu^{II}L_2(SCN)_5]_n$

The synthesis of the $[Cu^{I}_3Cu^{II}L_2(SCN)_5]_n$ was carried out by slow diffusion. To do this, after having dissolved 20 mg of potassium thiocyanate KSCN (0.2 mmol) in 15 ml of distilled water in a Pyrex glass-tube, a phase of acetonitrile and water CH_3CN / H_2O (v/v : 1/1, 15 ml) is added dropwise. Subsequently, 24 mg of the ligand L (0.1 mmol) and 17 mg of $CuCl_2 \cdot 2H_2O$ (0.1 mmol) dissolved in 15 ml of acetonitrile are carefully added to the previous solution. The tube is closed with parafilm and left at room temperature. After three months, brown crystals appeared. The obtained product is filtered, washed with water and ether and then dried under vacuum. Yield: 63% (based on Cu). Anal. Calcd. (%) for $C_{25}H_{16}Cu_4N_{13}S_7$: C, 30.73; H, 1.65; N, 18.64; S, 22.97. Found (%):C, 30.92; H, 1.71; N, 18.89; S, 23.2. FTIR (KBr pellet, cm^{-1}): 2221 (vs), 2101 (vs), 2068 (vs), 1635 (m), 1603 (m), 1434 (m), 1032 (w), 742(s). UV-vis (λ_{max}, nm (ε_{max}, $M^{-1}cm^{-1}$) in DMSO (10^{-4} M): 699 (520), 606 (1145), 536 (310), 403 (830), 313(17380), 271 (12920).

2.2. X-ray data collection and crystal structure determination

A suitable single crystal for X-ray diffraction analysis of the title compound was selected under a microscope (0.26 × 0.24 × 0.18 mm). The red single crystal for the X-ray diffraction (XRD) data collection was mounted on a Bruker X8 four circle diffractometer equipped with a CCD bi-dimensional detector and MoK_α graphite-monochromatic radiation (λ = 0.71073 Å). Data was corrected for Lorentz and polarization effects and for absorption [48,49]. The structure was solved by direct methods using SHELXT [50] and refined (by weighted full matrix least-square on F^2 techniques) to convergence using the SHELXL2014

program [51]. The plot of the title complex and the three-dimensional drawing of the crystal structure are obtained using the Ortep3 and Mercury programs, respectively [52,53].

2.3. Physical measurements

FTIR spectra were recorded on a SHIMADZU FT-IR 8400S spectrometer with samples dispersed in KBr pellets in the range 500-4000 cm^{-1}. UV-Visible absorption spectra in dimethyl sulfoxide (DMSO) solvent were recorded in the range 200-800 nm using a SHIMADZU 2450 spectrophtometer. Element analyses (C, H, N and S) were performed on a VARIO-ELEMENTAR analyzer.

Magnetic measurements (thermal dependence of the susceptibility and field dependence of the magnetization) have been collected using the VSM module of a Physical Property Measurement System (PPMS) Dynacool, maximum field = 9T.

2.4. Hirshfeld surface analysis

The Hirshfeld surfaces of $Cu^{I}_{3}Cu^{II}(SCN)_5L_2$ complex were analyzed so as to clarify the nature of the intermolecular interactions. Thus, a Hirshfeld surface analysis [54] and the associated two-dimensional fingerprint plots [55] were performed using CrystalExplorer17.5 [56] to figure out the normalized contact distance (d_{norm}), which depends on contact distances to the closest atoms outside (d_e) and inside (d_i) the surface. The 3D d_{norm} surfaces are mapped over a fixed colour scale of -0.6711 to 1.0573 for $Cu^{II}L_2(SCN)_2$, and shape index mapped in the colour range of -1.0 to 1.0 a.u.

2.5. *In vitro antimicrobial activity*

Antifungal screening was performed against three strain of *Verticillium dahliae* (SE, SH and SJ), previously isolated from olive trees in different region in Morocco and one isolate of

Fusarium oxysporum fsp. *melonis* (FOM). They were sub-cultured on potato dextrose agar (PDA) plates at 27°C in the dark. The polymer was dissolved in 0.2% DMSO and added at concentrations of 50, 100 and 200 µg mL^{-1} to the PDA medium before being autoclaved and cooled. The amended media was poured into Petri dishes and inoculated using 5 mm plugs of agar and mycelium taken from actively growing cultures of fungus on PDA. Petri plates were incubated in the dark at 27°C. The mycelial growth was assessed by measuring 2 orthogonal diameters of each colony after 7 days of incubation. Mycelial growth was compared with growth on PDA amended with 0.2% DMSO (control) and the percentage of inhibition growth was expressed [57] relative to the control. The experiment was repeated 3 times.

The *in vitro* antibacterial screening of the polymer was assessed against *Agrobacterium tumefaciens* (Ach5, A281 and C58 strains), *Pseudomonas syringae* pv. *tabaci* (strain CFBP2106) and *Pseudomonas syringae* pv. *syringae* (strain CFBP692). *A. tumefaciens* strains were sub-cultivated on LB solid medium while *P. syringae* pv. *syringae* and *P. syringae* pv. *tabaci* were cultured on King B (KB) medium at 28°C. Antibacterial activity of the polymer was investigated using the agar disc diffusion method as described previously [58]. Bacteria that were grown overnight were diluted to a concentration of 3×10^8 CFU. mL^{-1}. Sterile cellulose discs of 6 mm diameter were impregnated with the polymer (200 µg mL^{-1} in 0.2% DMSO) or with DMSO (0.2%), which was used as a negative control. The inoculated plates were incubated at 28°C for 48 h. The antimicrobial activity was evaluated by measuring the clearance zone around the discs which indicates a positive antibacterial activity of the respective products. Each experiment was repeated 3 times.

All data were expressed as the mean and confidence intervals. Data were subjected to ANOVA, and means were compared using Tukey's test and *p* values of 0.05 were considered to be significantly different.

3. Results and discussion

3.1. Crystal structure description and discussion

The mixed-valence copper coordination polymer, $[Cu^{I}_{3}Cu^{II}L_2(SCN)_5]_n$, was obtained by reaction between the thiadiazole ligand (L), $CuCl_2{\cdot}2H_2O$ and KSCN in H_2O/CH_3CN solution (see Scheme 2). The copper polymeric complex crystallizes in monoclinic symmetry and *C* 2/*c* space group with three independent copper crystallographic sites, and the crystal structure plot of the asymmetric unit is shown in Fig. 3, which leads to the chemical formula $[Cu^{I}_{3}Cu^{II}L_2(SCN)_5]_n$ with mixed valence of copper. The crystal structure determination details of copper complex are given in Table 1, with atomic positions, isotropic thermal displacement factors, selected bond lengths and angles given in Tables S1-S3 of supplementary information file. Hydrogen atoms were positioned in idealized positions and included in the final cycles of refinement with isotropic thermal parameters yielding the final R_1 = 3.82 % and wR_2 = 9.53 % for all 3076 unique reflections. The hydrogen bonds C–H···N are reported in Table 2.

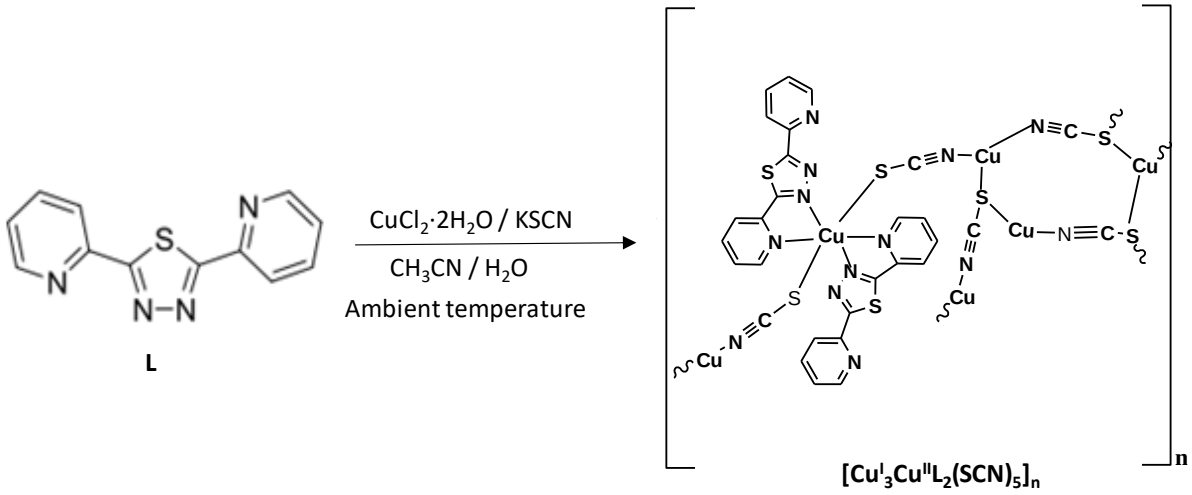

Scheme 1. In situ formation of $[Cu^{I}_{3}Cu^{II}L_2(SCN)_5]_n$.

The bidentate 1,3,4-thiadiazole ligand substituted by two 2-pyridyl rings has been found to produce the new monomeric complex. The 1,3,4-thiadiazole and pyridyl rings surrounding the Cu atom, in addition to the non-coordinated pyridyl ring are almost coplanar with the

maximum deviation from the mean plane of -0.089 Å at Cu1. The divalent copper cation Cu1 located on symmetry center is connected to two 1,3,4-thiadiazole ligands via the nitrogen atoms in equatorial positions and to two thiocyanate anions in axial positions. As a result, each copper (II) atom is in an octahedral geometry as shown in Fig. 4. The structure also contains three units [CuISCN] whose the monovalent copper atoms Cu2 and Cu3 have S2N2 and S2N environments respectively. The copper cations are connected by two thiocyanate ligands in μ-1,3-SCN coordination mode. The third thiocyanate ligand exhibits a μ-1,1,3-SCN coordination mode. The Cu2 is linked to four thiocyanate molecules. The coordination sphere around the metal center consists of two nitrogen atoms (N5 and N6) and two sulfur atoms (S4 and S3vi) building a distorted tetrahedron. Polyhedron angles exhibit a remarkable deviation from a perfect tetrahedron and their values are in range from 105.81 (6) to 116.19 (14) °. The Cu2–N5 and Cu2–N6 bond lengths are of 1.96 and 1.98 Å, respectively, while the distances Cu2–S3 and Cu–S4 are equal to 2.39 and 2.30 Å, respectively. The monovalent copper cation Cu3 is in a planar trigonal geometry (Fig. 4). However, the geometry is not ideal since the two Cu–S bonds are almost equal to 2.129 (15) Å) and larger than the third Cu–N bond which is equal to 1.908 (6) Å. The S–Cu–S angles are on the order of 130 °, being larger than the other two N–Cu–S angles which are both equal to 115 °.

The most interesting characterization of the structure of $[Cu^{I}_{3}Cu^{II}L_2(SCN)_5]_n$ is the formation of 2D honeycomb layers by $[Cu^{I}(SCN)]$ units (Fig. 5). As a result, a 3D architecture is formed with the molecules $[Cu^{II}L_2(SCN)_2]$ which are sandwiched between these layers and whose thiocyanate ligands connect them to the 2D sheets (CuSCN) through their atom. nitrogen. The planar $[Cu^{II}L_2(SCN)_2]$ moieties stacking along b axis are linked together by π–π stacking interaction between pyridine rings with intercentroid distance of 3.844(2) Å as shown in the perspective view of the crystal structure of this complex in Fig. 6.

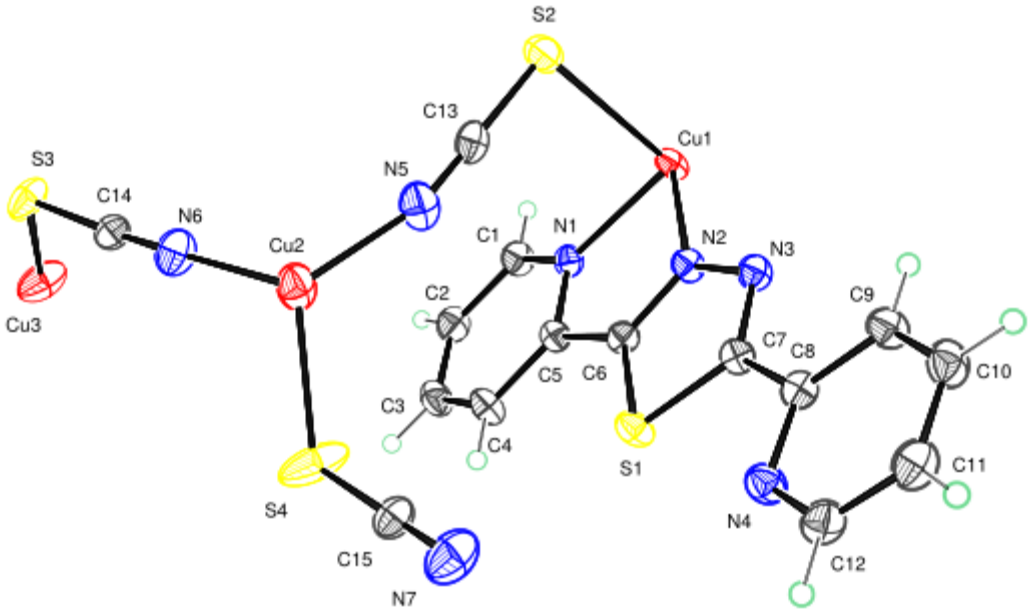

Fig. 3. Plot of the crystal structure of $[Cu^{I}_{3}Cu^{II}L_{2}(SCN)_{5}]_{n}$, with the atom-labelling scheme of the asymmetric unit. Displacement ellipsoids are drawn at the 50% probability level. H atoms are represented as small circles.

Table 1
Crystal data and summary of the measurement parameters for $[Cu^{I}_{3}Cu^{II}L_2(SCN)_5]_n$.

Chemical formula	$C_{29}H_{16}Cu_4N_{13}S_7$
M_r (g mol^{-1})	1025.13
Crystal system, space group	Monoclinic, *C*2/*c*
Temperature (K)	173
a, *b*, *c* (Å)	11.4672 (4), 11.1360 (4), 27.5492 (9)
β (°)	90.971 (2)
V (Å^3)	3517.5 (2)
Z	4
Radiation type	Cu K_α
μ (mm^{-1})	7.00
Crystal size (mm)	0.26 × 0.24 × 0.18
Data collection	
Diffractometer	Bruker D8 VENTURE Super DUO
Absorption correction	Multi-scan (*SADABS*; Krause *et al.*, 2015)
T_{min}, T_{max}	0.348, 0.753
No. of measured, independent and observed [$I > 2\sigma(I)$] reflections	32897, 3076, 2878
R_{int}	0.037
(sin $\theta/\lambda)_{max}$ (Å^{-1})	0.593
Refinement	
$R[F^2 > 2\sigma(F^2)]$, $wR(F^2)$, *S*	0.038; 0.097; 1.12
No. of reflections	3076
No. of parameters	243
H-atom treatment	H-atom parameters constrained
	$w = 1/[\sigma^2(F_o^2) + (0.0328\ P)^2 + 26.7834\ P]$ where $P = (F_o^2 + 2F_c^2)/3$
$\Delta\rho_{max}$, $\Delta\rho_{min}$ (e Å^{-3})	1.01, -0.99

Table 2
Hydrogen-bond geometry (Å, º) for $[Cu^{I}_{3}Cu^{II}L_2(SCN)_5]_n$.

D–H···*A*	*D*–H	H···*A*	*D*···*A*	*D*–H···*A*
C1–H1···N3^{i}	0.95 (??)	2.35 (??)	3.146 (5)	141
C2–H2···C13	0.95	2.64	3.55	177
C11–H11···C13	0.95	2.63	3.50	153
C4–H4···S3	0.95	2.89	3.67	140
C94–H9···S2	0.95	2.85	3.49	126

Symmetry code: (i) -*x*+1, -*y*+1, -*z*+1.

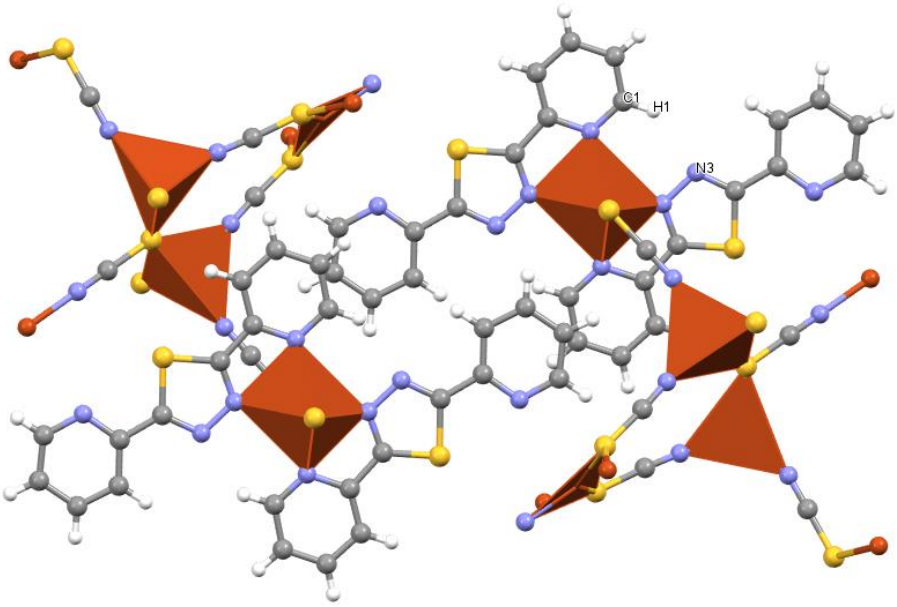

Fig. 4. ??????????????????????????????????????.

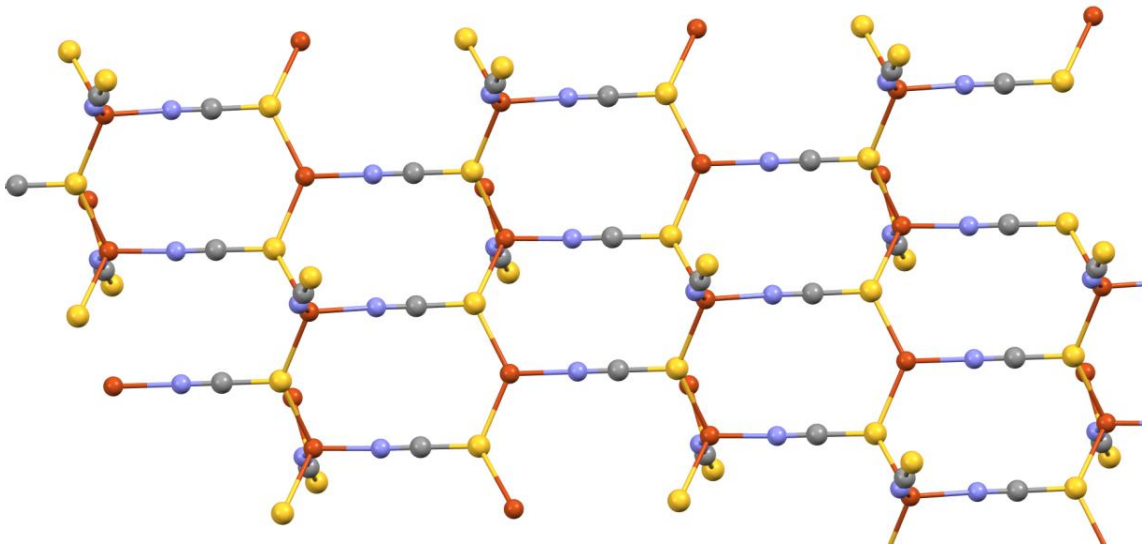

Fig. 5. ??????????????????????????????????????.

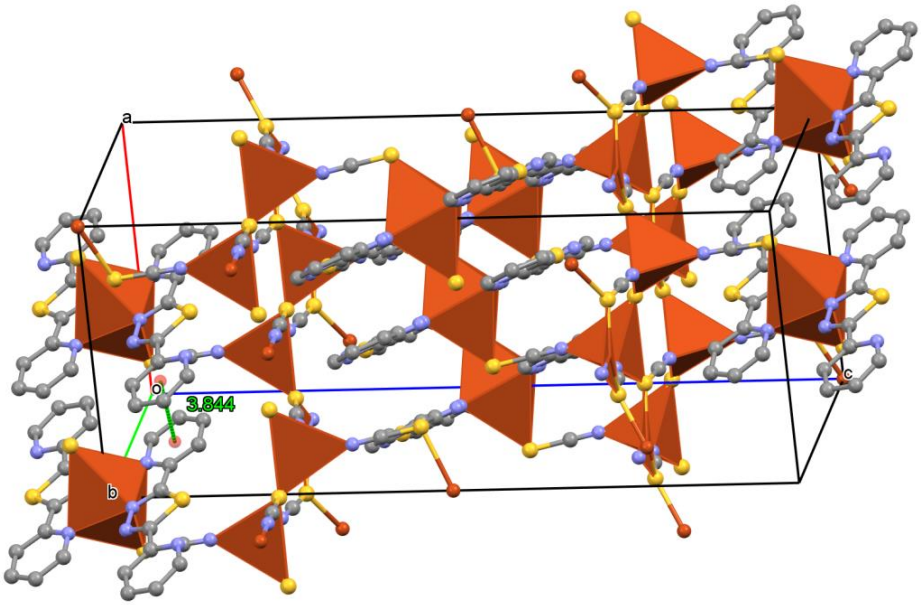

Fig. 6. ??????????????????????????????????????.

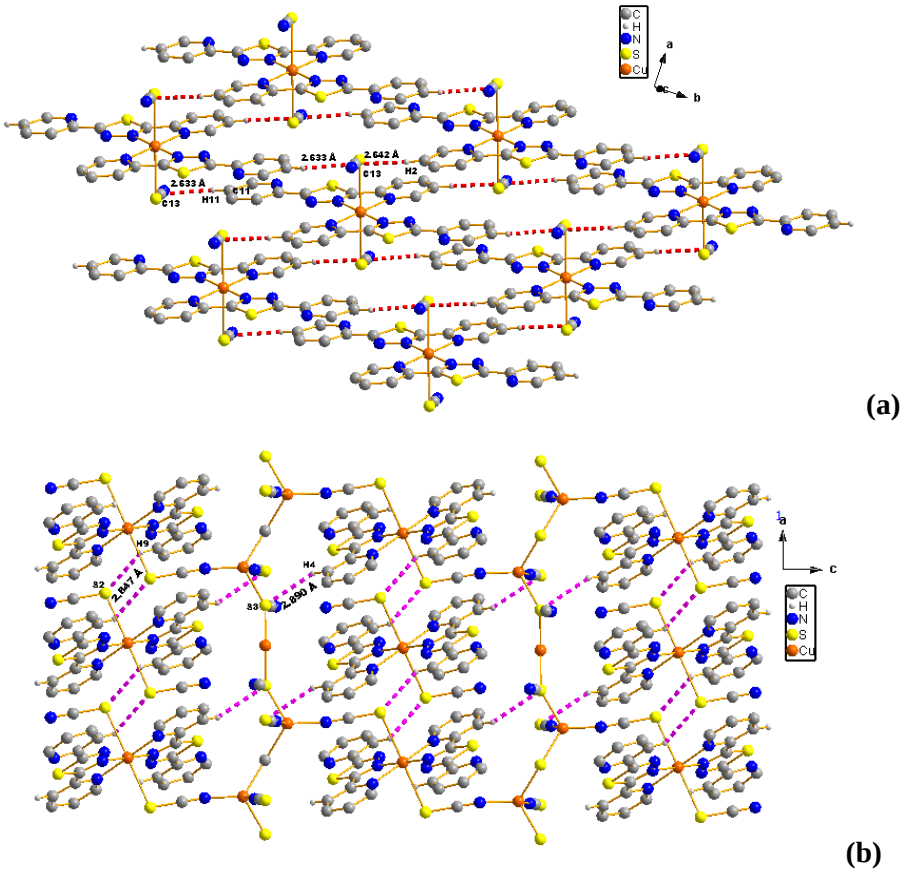

Fig. 6. a) C–H···C and b) C–H···S hydrogen-interactions in crystal structure of $[Cu^{I}_{3}Cu^{II}L_{2}(SCN)_{5}]_{n}$.

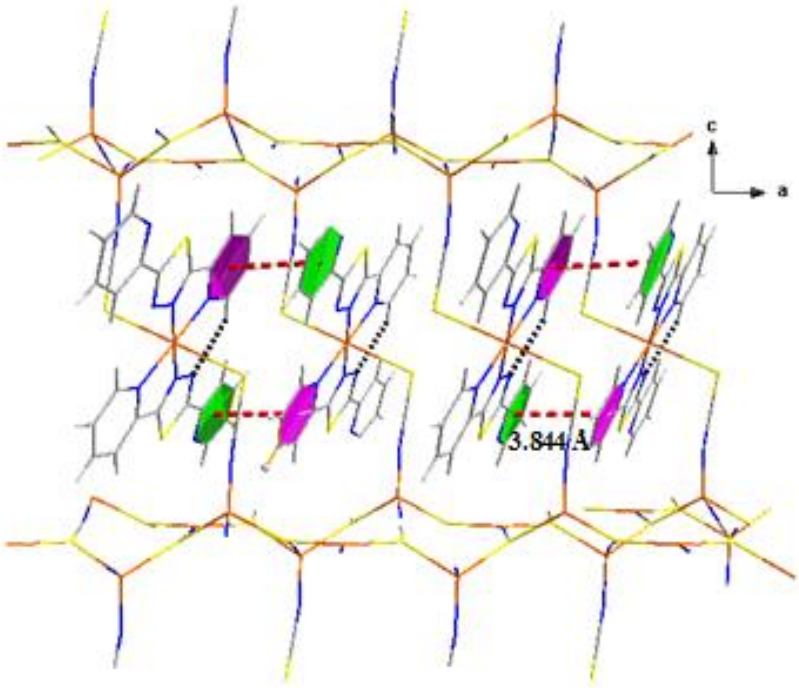

Fig. 7. Crystal packing of $[Cu^{I}_{3}Cu^{II}L_{2}(SCN)_{5}]_{n}$ showing C–H···N hydrogen interactions and the intermolecular π–π interactions between pyridyl rings.

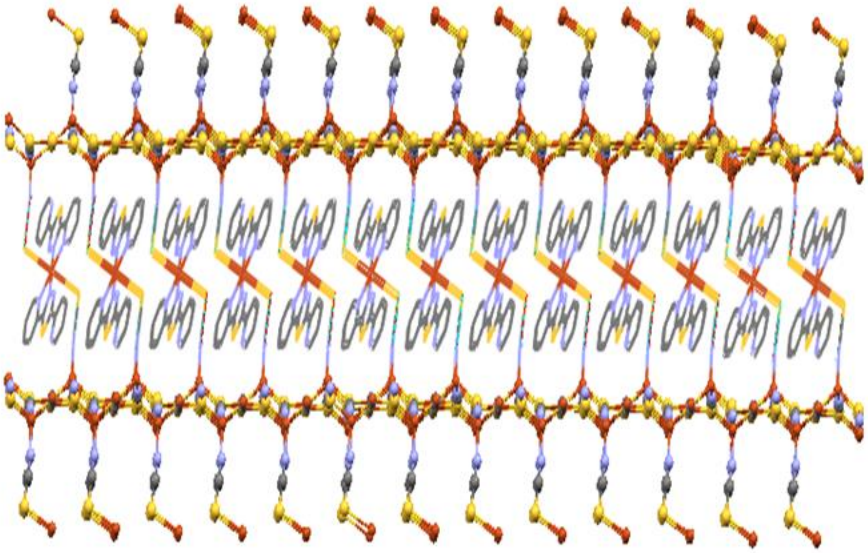

3.2. Hirshfeld surface analysis

Hirshfeld surface (HS) analysis and two-dimensional fingerprint plots generated using *CrystalExplorer17.5* shows the various intermolecular interactions in crystal structure (Fig. 8). d_{norm} and shape-index are mapped over the Hirshfeld surface for the $[Cu^{I}_{3}Cu^{II}L_2(SCN)_5]_n$ complex. The red spots on the Hirshfeld surface mapped with d_{norm} correspond to the C–H···C, C–H···S hydrogen bond and π–π stacking interactions. The most closet interactions refer to the Metal–S interactions, as they are indicated by the deep red regions on d_{norm} surface, near the metal atoms.

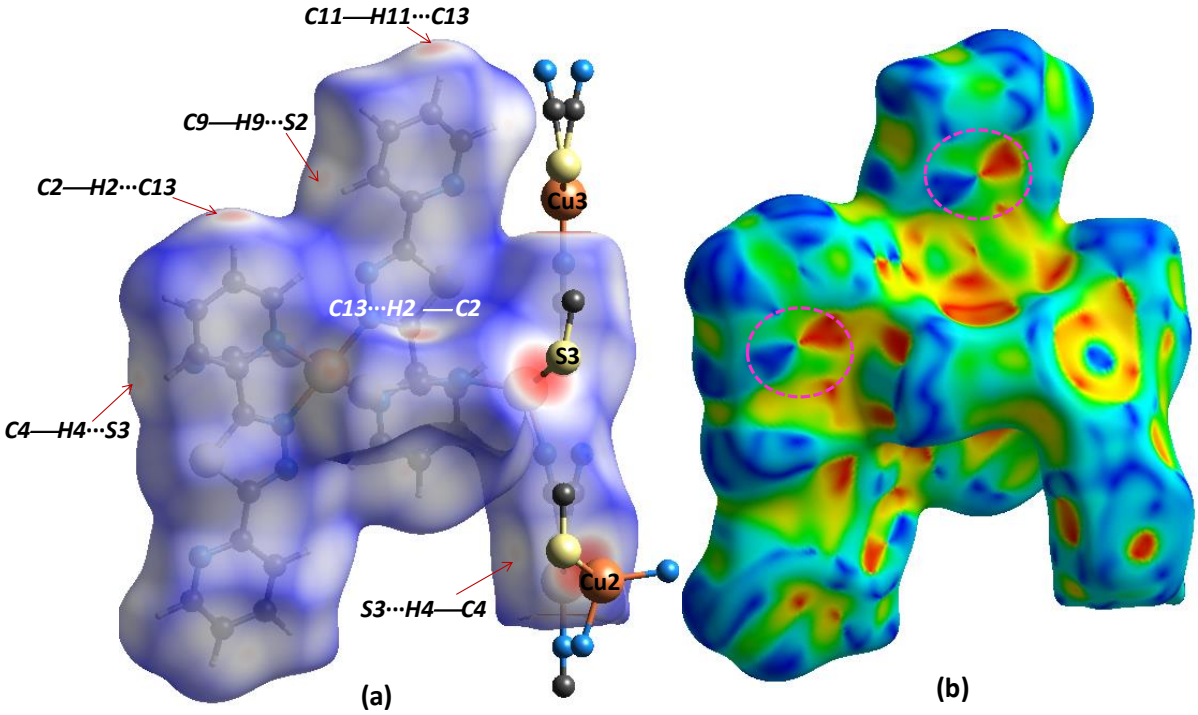

Fig. 8. Views of the Hirshfeld surfaces of $[Cu^{I}_{3}Cu^{II}L_2(SCN)_5]_n$ complex plotted over (a) d_{norm} and (b) shape-index map.

As illustrated in Fig. 9, the corresponding fingerprint plots for the title compound are shown with characteristic pseudo-symmetric wings in the d_e and d_i diagonal axes and those delineated into H···C/C···H, N···H/H···N, S···H/H···S, C···C, H···H, S···Cu/Cu···S, N···Cu/Cu···N and N···S/S···N. The relative contributions of all the contacts to the Hirshfeld surface are summarized in Table S4. The C···H/H···C interactions 24.6% interactions, corresponding to C11–H11···C13 and C2–H2···C13 interactions between 1,3,4-thiadiazole ligands and thiocyanate anions, is represented by the spikes in the bottom right and left region, $d_e + d_i \approx 2.5$ Å (Fig. 9b). The smaller red spot in the d_{norm} map show weak S···H/H···S, contacts attributed to C9–H9···S2 and C4–H4···S3 hydrogen bonds with notable contribution of 16.4% to the Hirshfeld surface area (Fig. 9c). The H···N/N···H contacts have significant contribution to the crystal packing where the distance $d_e + d_i \approx 2.6$ Å (Fig. 9d), arising from short interatomic H···N/N···H contacts. The distribution of points in the $d_e = d_i \approx 1.65$ Å range in the fingerprint plot delineated into C···C contacts (Fig. 9e), indicates the existence of weak π–π stacking interactions between the pyridyl (N1, C1–C5) and (N4, C8–C12) rings. The π–π interaction is indicated by adjacent red and blue triangles in the shape-index map (Fig. 8b). The H···H contacts (9.9 % contribution), Fig. 9f, represent van der waals interactions. The small contributions from other remaining interatomic contacts have negligible effect on the packing (Table S4).

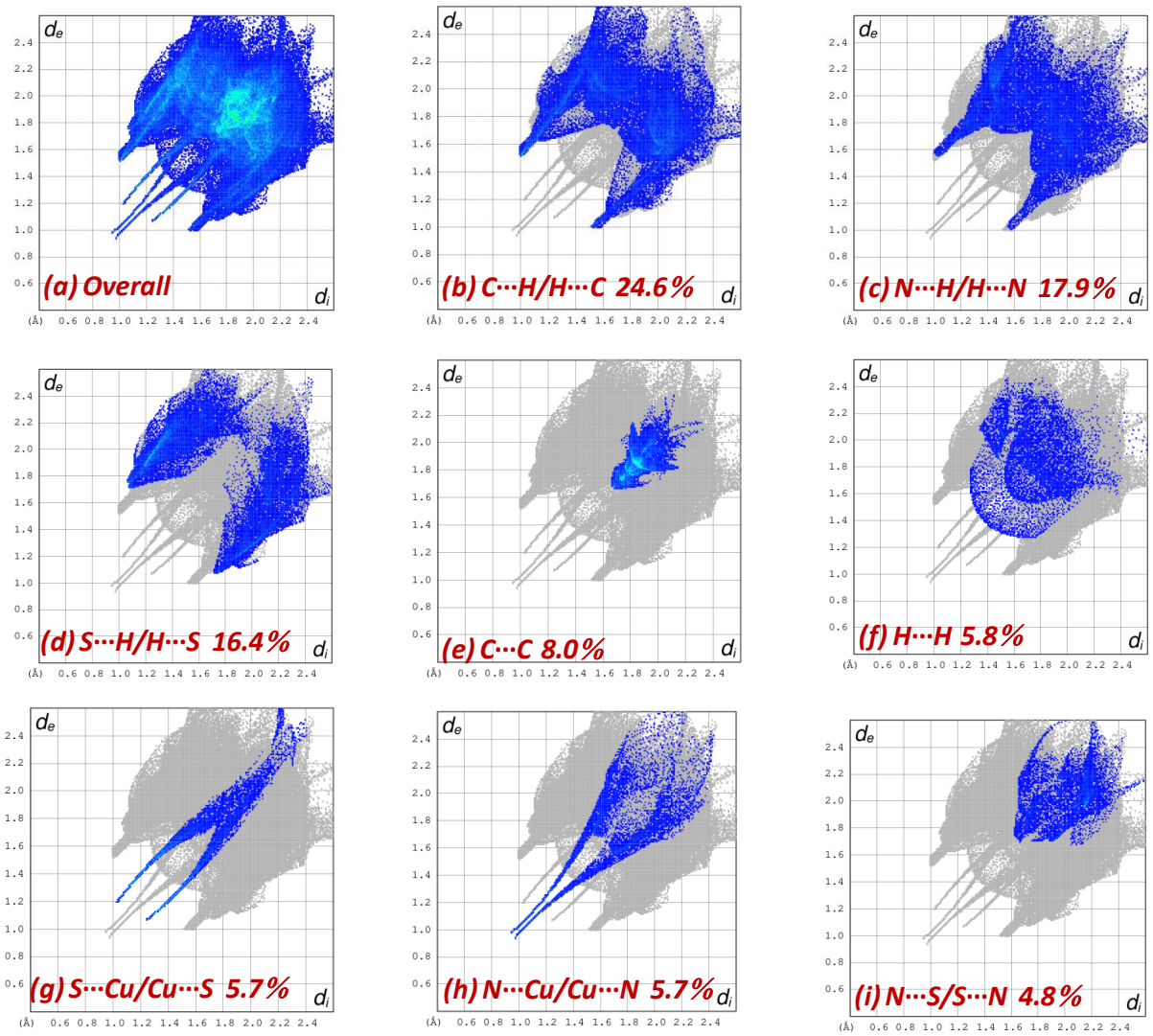

Fig. 9. a) The overall two-dimensional fingerprint plot of the $[Cu^{I}_{3}Cu^{II}L_2(SCN)_5]_n$ complex, and those delineated into: b) H···C/C···H, c) H···N/N···H, d) H···S/S···H, e) C···C, f) H···H, g) Cu···S/S···Cu, h) Cu···N/N···Cu and i) N···S/S···N.

The different coordination geometries about the metal centres have been mapped to a normal surface (d_{norm}) and are also reflected in the two-dimensional fingerprint plots shown in Fig. 10. All investigated surfaces differ in shape, indicating that the polyhedrons display different coordinations of all Cu ions, octhahedral for Cu^{II}, tetrahedral and trigonal for Cu^{I} (**Fig. 6 cristallo**). The HS mapped onto d_{norm} for the Cu(1) cation in $[Cu^{I}_{3}Cu^{II}L_2(SCN)_5]_n$ complex is a rectangular area, with the intense red spots corresponding to its coordinate bonds, which correlates with its octahedral geometry CuN_4S_2. Although the covalent bonds with the nitrogen atoms are dominant. The pale-red region displays the Cu···S contact (the bond length for S2–

Cu equal 2.803 Å). The 2D fingerprint plots of the interatomic interactions in the region of Cu(1) atom indicate that the Cu(1) atom has up to 79.7% of the contacts from the N–Cu interaction on the Hirshfeld surface (the pair of aligned red points at different inclinations from $d_e + d_i \approx 2.0$ Å) followed by 20.3% of the contacts from the S–Cu coordinates ($d_e + d_i \approx 2.8$ Å).

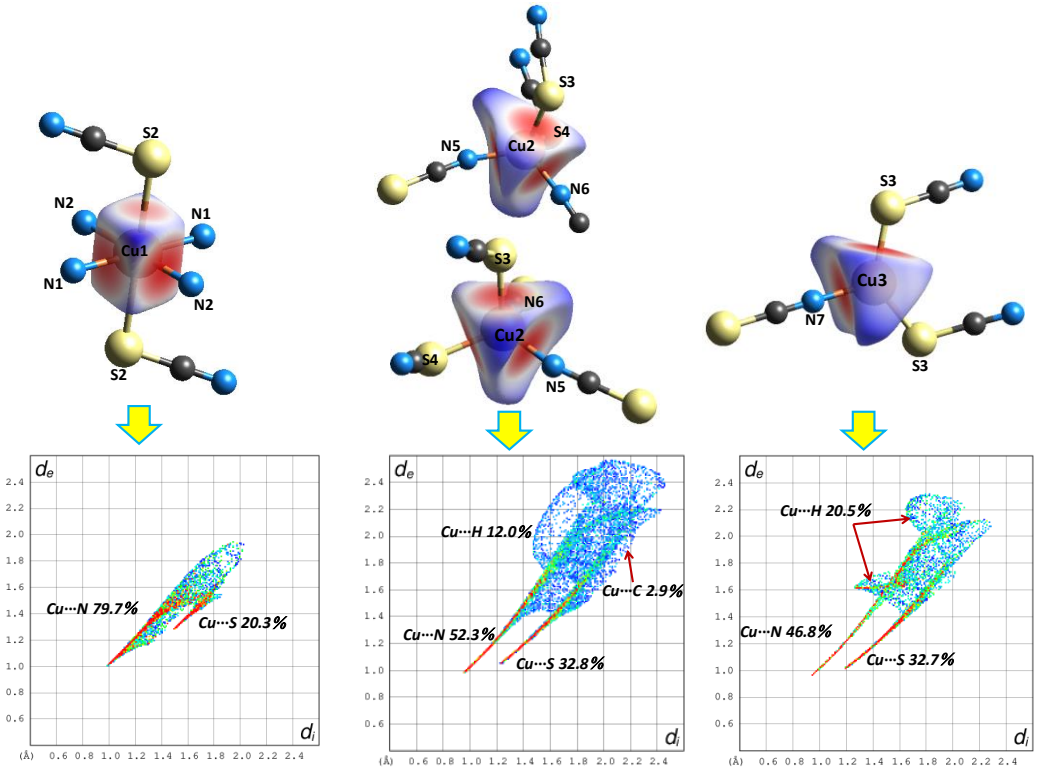

Fig. 10. Atomic Hirshfeld surface of Cu in $[Cu^{I}_3Cu^{II}L_2(SCN)_5]_n$ with the descriptor 'd_{norm}' mapped onto the surfaces and b) corresponding fingerprint plot for the metal atom (Cu).

The dark red regions on the d_{norm} surface for Cu(2) and Cu(3) show the contact between N–Cu and Cu···S. Although the covalent bonds with the nitrogen and sulfur atoms are dominant. The HS of the Cu^+ ion is much more concave towards the bond Cu–N than those associated with coordination towards the S atoms. With increasing contribution of Cu···N contacts, we observe diminishing contribution of the scattered spots, following the Cu···H interactions (12.0% and 20.5% for Cu2 and Cu3, respectively), while this interaction is absent in Cu(1). Moreover, the fingerprint for Cu(2) revealed the presence of Cu···C contacts at the

level 2.9%, while in Cu(1) and Cu(2) the contributions of similar contacts are absent. The HS of the metal centre differentiates relatively strong bonds from weaker contacts taking place within the interaction sphere.

3.3. Spectroscopy results

3.3.1. Ultraviolet-visible study

Characterization of the ligand L and $[Cu^{I}_{3}Cu^{II}L_{2}(SCN)_{5}]_{n}$ by UV-visible absorption spectroscopy in DMSO at room temperature is shown in Fig. 11. The absorption maxima with the corresponding extinction coefficients of both compounds are given in Table S5. In the ultraviolet domain, the electron spectrum of the title complex is characterized by the presence of two bands located at 313 and 271 nm. The similarity of this spectrum with that of the free ligand suggests that these two bands are assigned to the intraligand transitions $n \rightarrow \pi^*$ and $\pi \rightarrow \pi^*$ respectively [23,28,34]. In the visible range, the spectrum shows the presence of three low-intensity bands at 403, 536, 606 nm which can be attributed to the LMCT or MLCT transitions [59,60]. The spectrum also shows the presence of a band at 699 nm characteristic of a d-d electronic transition of a Cu(II) ion of configuration d^9 electronics adopting octahedral coordination geometry [61].

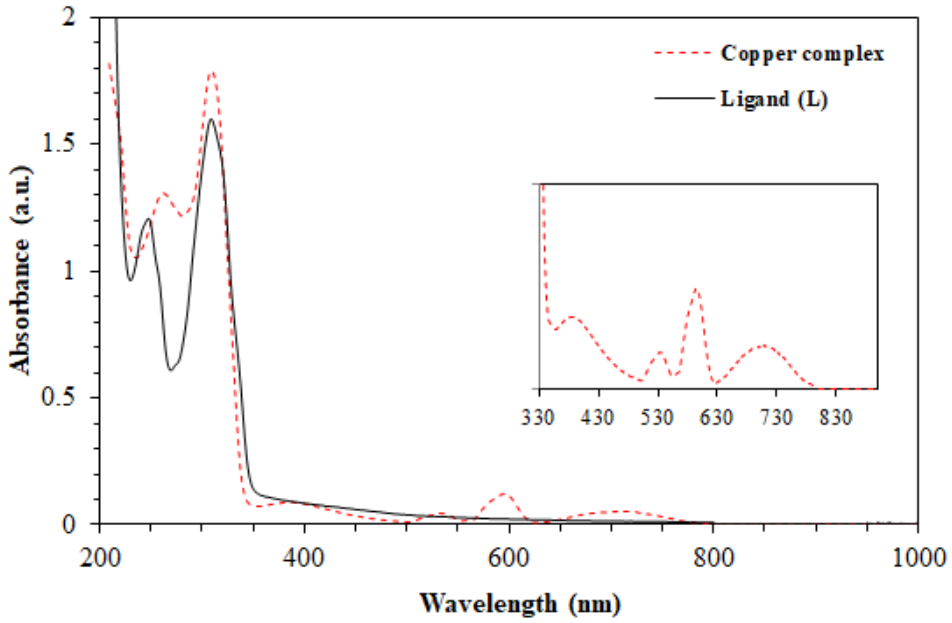

Fig. 11. Electronic spectra of the ligand L and its complex $[Cu^{I}_{3}Cu^{II}L_2(SCN)_5]_n$.

3.3.2. FTIR spectroscopy

The FTIR spectra of L and its copper complex are shown in Fig. 12 and the corresponding data are summarised in Table S6. The infrared spectrum of $[Cu^{I}_{3}Cu^{II}L_2(SCN)_5]_n$ shows the presence of three bands in the region [2050-2150] which correspond to the vibrations ν(CN) of the thiocyanate groups. The values of these bands are of the order of 2121, 2101 and 2068 cm^{-1}, which suggest the presence of three types of thiocyanate group in the isolated product. The spectrum also reveals the presence of the bands located around 1635, 1603 and 657 cm^{-1} which correspond respectively to ν(C=N), ν(C=C) and ν(C–S–C). These latter bands suggest the presence of the organic ligand [23,28,34] and its coordination to the metal center is confirmed by a band appearing at 564 cm^{-1} attributed to the Cu–N stretching [23].

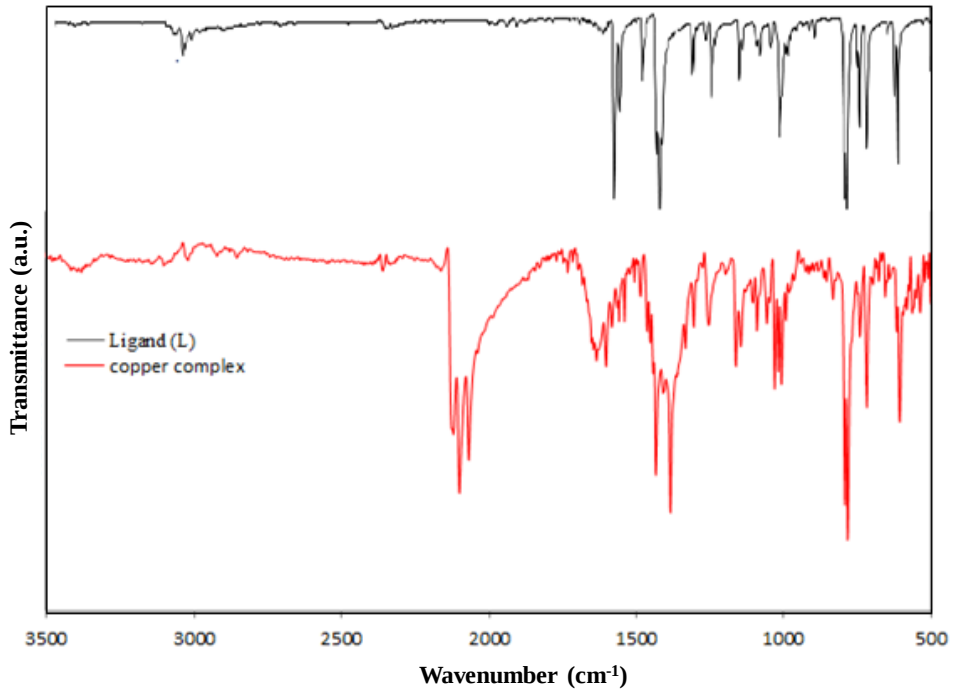

Fig. 12. Infrared spectra of ligand (**L**) and its complex $[Cu^{I}_{3}Cu^{II}L_{2}(SCN)_{5}]_{n}$ in the 500-3500 cm^{-1} range.

3.4. Magnetic properties

3.6. Antimicrobial activities

The effect of the polymeric complex $[Cu^{I}_{3}Cu^{II}L_2(SCN)_5]_n$ was assessed through the mycelial growth inhibition of 3 strains of *Verticillium. dahliae* (strains SE, SH and SJ) and one strain of *Fusarium oxysporum* fsp. *melonis*. Both pathogens are the causal agent of wilt that affects numerous crops of economic interest [62,63]. Its effect on radial growth (Table 3) showed no inhibition of mycelial growth whatever the concentration used and the fungal strain or species, although a moderate inhibition of the strains SE and SJ was observed with the highest concentration (200 µg mL^{-1}).

Table 3

In vitro inhibition of mycelial growth of *Fusarium oxysporum* fsp *melonis* and the strains SH, SE and SJ of *Verticillium dahlia*.

Concentration (µg mL^{-1})	Vd SH (%)	Vd SE (%)	Vd SJ (%)	FOM (%)
50	6 ± 1^a	23 ± 3^a	14 ± 9^a	4 ± 2^a
100	9 ± 3^a	27 ± 3^a	18 ± 6^a	10 ± 4^a
200	12 ± 2^a	29 ± 4^a	22 ± 5^a	13 ± 3^a

Data are means and confidence intervals from three replicates (a = 5%). Percentage of inhibition growth was determined at 7 days after incubation. Letters indicate significant differences within each treatment group according to Tukey HSD test ($P < 0.05$).

The effect of the polymer $[Cu^{I}_{3}Cu^{II}L_2(SCN)_5]_n$ was assessed through the mycelial growth inhibition of 3 strains of *Verticillium. dahliae* (strains SE, SH and SJ) and one strain of *Fusarium oxysporum* fsp. *melonis*. Both pathogens are the causal agent of wilt that affects numerous crops of economic interest [64,65].

In this study we also evaluated the effect of the polymer $[Cu^{I}_{3}Cu^{II}L_2(SCN)_5]_n$ against several phytopathogenic bacteria of economic interest including *A. tumefaciens,* which is the causal agent of crown gall disease [64]. A significant inhibition of the strains A281and Ach5 was observed. However, no significant inhibition was recorded against the strain C58, which is

the most virulent among the three strains, studied (Fig. 13). Similar results were obtained against *Pseudomonas syringae* pv. *syringae* and *Pseudomonas syringae* pv. *tabaci*, which are taxonomically related, but they differ in pathology, virulence and symptoms development in various crops [65].

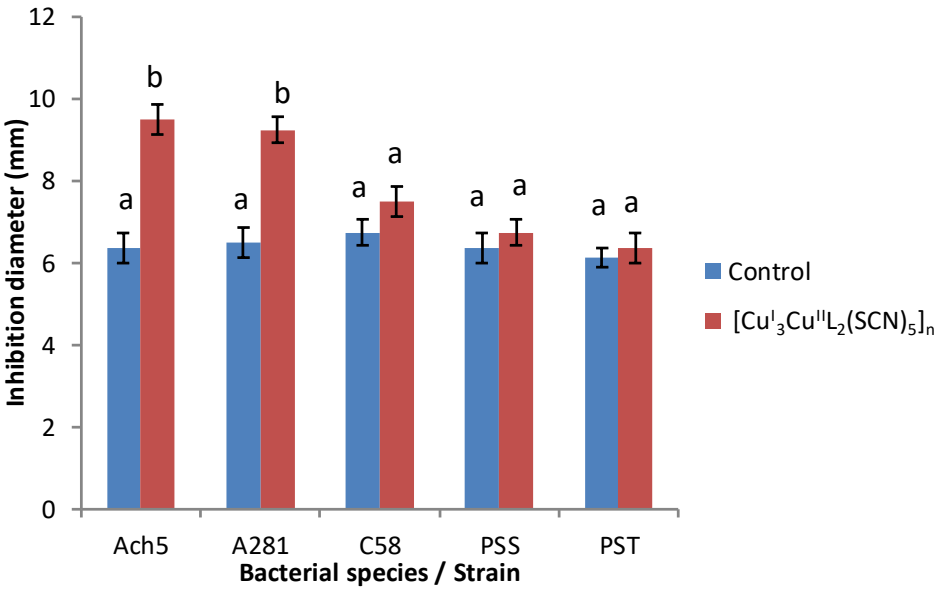

Fig. 13. Antibacterial activity of the mixed-valence coordination polymer, $[Cu^{I}_{3}Cu^{II}L_2(SCN)_5]_n$ against the strains Ach5, A281 and C58 of *Agrobacterium tumefaciens*, *Pseudomonas syringae* pv. *syringae* (PSS) and *Pseudomonas syringae*pv. *tabaci* (PST). Data are means and confidence intervals from three replicates (a = 5%). Inhibition diameter was recorded 48 h after incubation at 28 °C with sterile cellulose discs impregnated with 200 µg ml^{-1} of the polymer or with 0.2% DMSO used as a negative control. Letters indicate significant differences according to Tukey HSD test ($P < 0.05$).

4. Conclusion

???????

Supplementary material

CCDC ????? contains the supplementary crystallographic data for the asymmetric unit of $[Cu^{I}_{3}Cu^{II}L_{2}(SCN)_{5}]_{n}$. These data can be obtained free of charge via http://www.ccdc.cam.ac.uk/conts/retrieving.html, or from the Cambridge Crystallographic Data Centre, 12 Union Road, Cambridge CB2 1EZ, UK; fax: (+44) 1223-336-033; or e-mail: deposit@ccdc.cam.ac.uk.

Acknowledgement

The authors are greatly thankful to the CUR CA2D of Chouaib Doukkali University for its support and UATRS-CNRST for the use of the Bruker diffractometer.

References

[1] A. Liu, C.C. Wang, C.Z. Wang, H.F. Fu, W. Peng, Y.L. Cao, H.Y. Chu, A.F. Du, J. Colloid Interface Sci. 512 (2018) 730–739.
[2] A. Beheshti, K. Nozarian, N. Ghamari, P. Mayer, H. Motamedi, J. Solid State Chem. 258 (2018) 618–627.
[3] X. Zhang, X.L. Meng, C.M. Huang, G.H. Cui, J. Mol. Struct. 1100 (2015) 94–99.
[4] M. Song, B. Mu, R.D. Huang, J. Solid State Chem. 246 (2017) 1–7.
[5] X.Q. Zhao, Y.Y. Wang, S. Xiang, C. Lv, Y.J. Liu, F.S. Xu, D.X. Bao, J. Wang, Inorg. Chem. Commun. 85 (2017) 49–51.
[6] L.D. Rosales-Vázquez, V. Sánchez-Mendieta, I. García-Orozco, S. Hernández-López, D. Martínez-Otero, R.A. Morales-Luckie, R. Escudero, F. Morales, Inorg. Chim. Acta 471 (2018) 674–679.
[7] T.A. Makal, J. R. Li, W. Lu, H.C. Zhou, Chem. Soc. Rev. 41 (2012) 7761–7779.
[8] Y. He, W. Zhou, G. Qian, B. Chen, Chem. Soc. Rev. 43 (2014) 5657–5678.
[9] A.M. Banu, D. Friedrich, S. Brandani, T. Düren, Ind. Eng. Chem. Res. 52 (2013) 9946–9957.
[10] R.B. Lin, S. Xiang, H. Xing, W. Zhou, B. Chen, Coord. Chem. Rev. 378 (2019) 87–103.
[11] F. Dai, J. Dou, H. He, X. Zhao, D. Sun, Inorg. Chem. 49 (2010) 4117–4124.
[12] T.R. Cook, Y.R. Zheng, P.J. Stang, Chem. Rev. 113 (2012) 734–777.
[13] J. Ngoune, J.J. Anguile, J. Nenwa, G. Djimassinga, C. Pettinari, E. Álvarez, L. Pandolfo, Inorg. Chim. Acta 453 (2016) 263–267.
[14] D. Hursán, G. London, B. Olasz, C. Janáky, Electrochim. Acta 217 (2016) 92–99.
[15] E. Liu, H. Xiong, L. Li, C. Yang, Z. Yin, A. Chang, D.R. Manke. J.A. Golen, G. Zhang, Polyhedron 127 (2017) 355–360.
[16] K. S. Banu, S. Mondal, A. Guha, S. Das, T. Chattopadhyay, E. Suresh, E. Zangrando, D. Das, Polyhedron 30 (2011) 163–168.
[17] C.Y. Niu, B.L. Wu, X.F. Zheng, H.Y. Zhang, H.W. Hou, Y.Y. Niu, Z.J. Li, Cryst. Growth Des. 8 (2008) 1566–1574.
[18] Z. Huang, M. Du, H.B. Song, X.H. Bu, Cryst. Growth Des.4 (2001) 71–78.
[19] Z. Huang, H.B. Song, M. Du, S.T. Chen, X.H. Bu, J. Ribas, Inorg. Chem. 43 (2004) 931–944.
[20] C.Y. Niu, B.L. Wu, X.F. Zheng, X.S. Wan, H.Y. Zhang, Y.Y. Niu, L.Y. Meng, CrystEngComm. 11 (2009) 1373–1382.
[21] F. Bentiss, M. Lagrenée, O Mentré, P. Conflant, H. Vezin, J.P. Wignacourt, E.M. Holt. Inorg. Chem 43 (2004) 1865–1873.
[22] A. Laachir, F. Bentiss, S. Guesmi, M. Saadi, L. El Ammari, Acta Cryst. E69 (2013) m351–m352.
[23] A. Laachir, S. Guesmi, E.M. Ketatni, M. Saadi, L. El Ammari, S. Esserti, M. Faize, F. Bentiss, J. Mol. Struct. 1218 (2020) 128533.
[24] F. Bentiss, M. Lagrenée, J. P. Wignacourt, E.M. Holt, Polyhedron 21 (2002) 403–408.
[25] F. Bentiss, M. Lagrenée, H. Vezin, J.P. Wignacourt, E.M. Holt, Polyhedron 23 (2004) 1903–1907.
[26] X.F. Zheng, X.S. Wan, W. Liu, C.Y. Niu, C.H. Kou, Z. Kristallogr. NCS 221 (2006) 543–544.
[27] F. Bentiss, M. Outirite, M. Lagrenée, M. Saadi, L. El Ammari, Acta Cryst. E68 (2012) m360–m361.
[28] A. Laachir, S. Guesmi, M. Saadi, L. El Ammari, O. Mentré, H. Vezin, S. Colis, F. Bentiss, J. Mol. Struct. 1123 (2016) 400–406.
[29] A. Smaili, L.A. Rifai, S. Esserti, T. Koussa, F. Bentiss, S. Guesmi, A. Laachir, M. Faize, Pestic. Biochem. Physiol. 143 (2017) 26–32.
[30] A. Laachir, F. Bentiss, S. Guesmi, M. Saadi, L. El Ammari, Acta Cryst. E72 (2016) 1176–1178.
[31] A. Hazari, L.K. Das, A. Bauzá, A. Frontera, A. Ghosh, Dalton Trans. 43 (2014) 8007–8015.
[32] P. Saxena, J.M. Thomas, C. Sivasankar, N. Thirupathi, New J. Chem. 43 (2019) 2307–2327.
[33] F. Rhoufal, A. Laachir, S. Guesmi, L. Jouffret, N. Sergent, S. Obbade, M. Akkurt, F. Bentiss, ChemistrySelect 4 (2019) 7773–7783.
[34] A. Laachir, F. Rhoufal, S. Guesmi, E.M. Ketatni, L. Jouffret, N. Sergent, S. Obbade, F. Bentiss, J. Mol. Struct. 1208 (2020) 127892.
[35] F.A. Mautner, R.C. Fischer, A. Torvisco, M.M. Henary, F.R. Louka, S.S. Massoud, N.M. Salem, Molecules 25 (2020) 3376.
[36] B. Guo, X. Zhang, Y.N. Wang, J.J. Huang, J.H. Yu, J.Q. Xu, Dalton Trans. 44 (2015) 5095–5105.

[37] A. Hazari, S. Giri, C. Diaz, A. Ghosh, Polyhedron 118 (2016) 70–80.
[38] A. Espinosa, M. Sohail, M. Habib, K. Naveed, M. Saleem, H.U. Rehman, S. Ahmad, Polyhedron 90 (2015) 252–257.
[39] A. Biswas, R. Saha, A. Ghosh, CrystEngComm. 13 (2011) 5342–5347.
[40] L. K. Das, C. Diaz, A. Ghosh, Cryst. Growth Des. 15(2015) 3939–3949.
[41] A. G.Majouga, M.I. Zvereva, M.P. Rubtsova, D.A. Skvortsov, A.V. Mironov, D.M. Azhibek, O.O. Krasnovskaya, A.V. Udina, N.I. Vorozhtsov, E.K. Beloglazkina, L. Agron, L.V. Mikhina, A.V. Tretyakova, N.V. Zyk, N.S. Zefirov, A.V. Kabanov, O.A. Dontsova, J. Med. Chem. 57 (2014) 6252-6258.
[42] D. Anu, P. Naveen, B. VijayaPandiyan, C.S. Frampton, M.V Kaveri, Polyhedron 167 (2019) 137–150.
[43] L. Shi, P. Yang, G. Huang, Q. Li, N. Wang, J.Z. Wu, Y. Yu, J. Med. Chem. 184 (2011) 1699–1706.
[44] K. Himoto, S. Suzuki, T. Okubo, M. Maekawa, T. Kuroda-Sowa, New J. Chem. 42 (2018) 3995–3998.
[45] K. Nakatani, K. Himoto, Y. Kono, Y. Nakahashi, H. Anma, T. Okubo, M. Maekawa, T. Kuroda-Sowa, Crystals 5 (2015) 215-225.
[46] T. Okubo, H. Anma, Y. Nakahashi, M. Maekawa, T. Kuroda-Sowa, Polyhedron 69 (2014) 103–109.
[47] M. Lebrini, F. Bentiss, M. Lagrenée, J. Heterocycl. Chem. 42 (205) 991–994.
[48] Bruker, SAINT. Bruker AXS Inc., Madison, Wisconsin, USA, 2016.
[49] L. Krause, R. Herbst-Irmer, G.M. Sheldrick, D. Stalke, J. Appl. Cryst. 48 (2015) 3–10.
[50] G.M. Sheldrick, Acta Cryst. A71 (2015) 3–8.
[51] G.M. Sheldrick, Acta Cryst. C71 (2015) 3–8.
[52] L.J. Farrugia, J. Appl. Cryst. 45 (2012) 849–854.
[53] C.F. Macrae, I.J. Bruno, J.A. Chisholm, P.R. Edgington, P. McCabe, E. Pidcock, L. Rodriguez-Monge, R. Taylor, J. van de Streek, P.A. Wood, J. Appl. Cryst. 41 (2008) 466–470.
[54] M.A. Spackman, D. Jayatilaka, CrystEngComm. 11 (2009) 19–32.
[55] J.J. McKinnon, D. Jayatilaka, M.A. Spackman, Chem. Commun. (2007) 3814–3816.
[56] M.J. Turner, J.J. McKinnon, S.K. Wolff, D.J. Grimwood, P.R. Spackman, D. Jayatilaka, M.A. Spackman, CrystalExplorer17, The University of Western Australia, 2017.
[57] S.Z. Zhan, R. Peng, S.H. Lin, S.W. Ng, D. Li, CrystEngComm. 12 (2010) 1385–1387.
[58] A. Smaili, N. Mazoir, L.A. Rifai, T. Koussa, K. Makroum, A. Benharref, L. Faize, N. Alburquerque, L. Burgos, M. Belfaiza, M. Faize, Nat. Prod. Commun. 12 (2017) 331–336.
[59] S. Esserti, A. Smaili A, L.A. Rifai, T. Koussa, K. Makroum, M. Belfaiza, M. Kabil, L. Faize, L. Burgos, N. Alburquerque, M. Faize, J. Appl. Phycol. 29 (2017) 1081–1093.
[60] L. Li, A.R. Craze, D.J. Fanna, A.J. Brock, J.K. Clegg, L.F. Lindoy, J.R. Aldrich-Wright, J.K. Reynolds, F. Li, Polyhedron 125 (2017) 44-49.
[61] S. Jyothi, K. Sreedhar, D. Nagaraju, S.J Swamy, Can. Chem. Trans. 3 (2015) 368–380.
[62] T.R. Gordon, R.D. Martyn, Annu. Rev. Phytopathol. 35 (1997) 111–128.
[63] H. Zine, L.A. Rifai, T. Koussa, F. Bentiss, S. Guesmi, A. Laachir, K. Makroum, M. Belfaiza, M. Faize, Pest Man. Sci. 73 (2017) 188–197.
[64] E.E. Hood, G.L. Helmer, R.T. Fraley, M.D. Chilton, J. Bact. 186 (1986) 1291–1301.
[65] J.M. Young, D.W. Dye, J.F. Bradbury, C.J. Panagopoulos, C.F. Robbs, New Zeal. J. Agr. Res. 21 (1978) 153–177.